Editorial Team

JOURNAL OF CARDIOVASCULAR, NEUROVASCULAR & STROKE

Contents

No.   *Title*   *Page*

balt solutions
for AVM treatment

squid
EVOH co-polymer

sonic
detachable tip microcatheter

balt
inspiring innovation

Join us for Hands-On
AVM Workshops. Register your interest with
carlteh@medcinpharma.com / hiba@medcinpharma.com

EVALUATION OF INTRACEREBRAL HAEMORRHAGE'S SURFACE AREA USING ARTIFICIAL INTELLIGENCE IN COMPUTED TOMOGRAPHY

Azzam Basseri Huddin[1], Aqilah Baseri Huddin[2], Anas Tharek[*1], Wan Mimi Diyana Wan Zaki[2], Ahmad Sobri Muda[1]

[1]Department of Radiology, Hospital Pengajar Universiti Putra Malaysia, Universiti Putra Malaysia, Faculty of Medicine and Health Sciences, Universiti Putra Malaysia, Serdang, Malaysia
[2]Department of Electrical, Electronic and Systems Engineering, Faculty of Engineering and Built Environment, Universiti Kebangsaan Malaysia, Bangi, Malaysia

*Corresponding author:
Anas Tharek, Department of Radiology, Hospital Pengajar Universiti Putra Malaysia, Universiti Putra Malaysia, Faculty of Medicine and Health Sciences, Universiti Putra Malaysia, Serdang, Malaysia. Email: anastharek@gmail.com

ABSTRACT
Introduction: AI-based techniques can be used to localize and measure the intracerebral haemorrhage (ICH) in computed tomography (CT). This study aims to develop an automated detection algorithm with higher sensitivity in ICH evaluation in comparison to the conventional method. This indirectly influences the patient's prognosis by reducing the risk of delay or misdiagnosis.
Methods: Selected 50 CT brain images with primary ICH were used for three different measurement approaches including the conventional Kothari method (Conventional), AI-based method (A.I.), and manually marking by the radiologist, which is the ground truth (G.T.). In the automated system, a convolutional neural network (CNN) is used to localize the ICH, followed by a thresholding technique to segment the ICH, and finally, the measurements are computed. The segmentation performance is measured using Dice similarity coefficient. The automated ICH measurements are compared against the ground truth (A.I. vs G.T.). Concurrently, the ICH measurements calculated using the conventional method are also compared against the ground truth (Conventional vs G.T). The t-test analysis is performed between the sum squared error (SSE) of ICH measurements from the automated-ground truth and the conventional-ground truth.
Results: The mean volumetric Dice similarity coefficient for the automated segmentation algorithm when tested against the ground truth, is 0.859±0.135. The t-test analysis of the SSE between conventional-ground truth (median=5.45, SD=3.96) and automated-ground truth (median=0.73, SD=0.78) achieved p-value < 0.001 (p=5.10E-9).
Conclusion: The automated AI-based algorithm significantly improved the ICH surface area measurement from the CT brain with higher accuracy and efficiency in comparison to the conventional method.

Keywords: Artificial Intelligence; Machine learning; Radiology; Neurology; CT Brain

INTRODUCTION
One of the most common brain pathologies is intracranial haemorrhage. It is defined as any bleeding episode within the brain or cranial vault. It can be divided into a few categories, which are based on the acuteness of the blood formation and the spaces involved. This categorization is important, as it plays a crucial role in determining the severity of the bleeding and treatment options, as well as predicting the outcomes [1].

Based on brain locations or spaces the bleeding occurs, it can be divided into intra-axial and extra-axial haemorrhage. Intraaxial haemorrhage is defined as bleeding which occurs in the brain, which is intracerebral haemorrhage, while extra-axial haemorrhage is bleeding which occurs outside of the brain parenchyma, which is subdural, subarachnoid, and epidural haemorrhage. Worsening of the patient's condition is usually due to secondary complications from intracranial bleeding, such as increases in the intracranial pressure, hydrocephalus, and significant midline shift.

Thus, the initial treatment option is crucial in improving patient prognosis and outcomes. Hence, a supportive measure such as prompt brain screening using computed tomography (CT) or magnetic resonance imaging (MRI) scan is helpful, to prevent any delay management.

Meanwhile, implementing artificial intelligence, aiming to aid the radiologist or physician in the detection of intracranial haemorrhage [2], may further reduce the risk of delay or misdiagnosis.

METHODS
Study Design
This was a cross-sectional Computed Tomography (CT) head study using primary raw data, in which the data was obtained from patient who was admitted to Hospital Serdang and underwent a non-enhanced CT brain examination in Radiology Department for further investigation. The data was checked to comply with the inclusion and exclusion criteria before taken as samples for this study. No consent was taken as this is a retrospective study and all the data are anonymized to secondary data.

Sampling Method
The population of this study consists of patients who were admitted and underwent non-enhanced CT brain for intracerebral haemorrhage, and within the inclusion criteria. The patient would present with common symptoms, including headache, hypertension, loss of consciousness, vomiting, or neurological deficit. The sample includes CT brain with intracerebral haemorrhage (ICH). The sample of CT Brain also needs to have formal radiologist report, to prevent from using uncertain brain pathology as the subject. Other types of intracranial haemorrhage, such as epidural or subdural haemorrhage (EDH & SDH).

Sampling Size
This study aims to determine a high level of agreement between readings obtained from A.I. and conventional methods. It is recommended to pre-specify a high value (for intraclass correlation coefficient (ICC) at 0.90 in the null hypothesis and a higher value (for ICC) at 0.95 in the alternative hypothesis). This is to ensure that the study has indicated that a minimum level of agreement as shown by ICC = 0.90 is expected in the first place, but the aim is to establish that the targeted level of agreement should be much higher, as shown by the value of ICC which exceeds 0.95. Therefore, based on only two observations made on each subject, a sample size of at least 50 is required to achieve statistical significance for an alpha-value set to be 0.05 and with a power of more than 80.0% [3].

Data Collection, Instruments and Quality Control
The CT head was scanned using a CT machine (Siemens Somatom 128 Slices) located in the Radiology Department Hospital Serdang of patients who are having ICH and complying with inclusion criteria. Data or images were then transferred to GE Centricity PACS UV software (version 6.0). for viewing. This data is downloaded from the PACS system in DICOM format and kept on a workstation computer. Personal information was filtered out or deleted during the process to anonymize the subject. These data were duplicated and placed into three separate folders, which are for A.I.-based automated evaluation, manual demarcation (Ground Truth), and conventional measurement, derived from Kothari's ABC/2 method.

In this project, MATLAB (version R2020a Update 3) is used as the software for developing the algorithm with the license number 40925593.

MATLAB is a numeric programming platform widely used to program a complex computing model.

Intracranial Hemorrhage Measurement Method

Three types of ICH measurement techniques were conducted, which are conventional measurement derived from Kothari's method, a calculation from manual demarcation method, and fully automated measurement by A.I-based technique [4].

The calculation is derived from the ABC/2 method proposed by Kothari et al. in 1996. However, only the first step, which is the two dimensions were taken. They are the largest diameter (A) of hemorrhage on the axial slice, and the largest diameter (B) at 90 degrees to plane A as shown in **Figure 1**. The multiplication of these two dimensions is the estimated surface area of ICH. The reason for extracting only the first step of Kothari's method is because this study which only focuses on surface area measurement.

The manual measurement of ICH is made using RadiAnt (version 2020.1.1) or Osirix (version 11.0) viewer application. This software is compatible with Windows or Macintosh operating systems, respectively. In this viewer, the CT images are displayed, and the surface area was calculated manually by defining the length of A and B. However, this estimation is inaccurate since the formulation of A times B defines the area of a rectangle instead of the real area of ICH. The volume estimation using this method has been proven to demonstrate apparent inaccuracy, especially in significantly large hematoma, as it tends to underestimate its volume [5]. This has indirectly increased the odds of poor outcomes.

The second method for surface area measurement is performed in a hybrid way and hence the measurement is said to be 'semi-automatically' done. The ICH area is manually demarcated by the trained radiologists and the surface area is automatically calculated by the MATLAB software.

The demarcation process involved the conversion of CT images into compatible file types (JPEG), to be opened in photo editing software, which are Photos or Notability (version 10.4.2) applications on iPad Pro 10.1 (iPadOS 14). The margin is drawn by two different trained radiologists. **Figure 2** shows an example of two ICH markings from two different radiologists on the same CT image in red color ink.

The next step is to calculate the area of the marked ICH. The measurement is made using the MATLAB software by calculating number of pixels included in the marked area. The automated ICH measurement algorithm is implemented based on AI techniques. The algorithm includes 4 important steps, 1) pre-processing, 2) segmentation, 3) ICH localization and detection 4) measurement.

In the pre-processing step, the images were pre-processed and normalized via the histogram normalization technique. This step is performed to achieve a standard range of pixels value in all images from 0 (black) to 1 (white). This is important to ensure the consistency of data distribution in the dataset.

After an image is pre-processed, the next step is to exclude the outer skull by a segmentation process. The algorithm used for the segmentation step is known as pixel thresholding. In the thresholding method, the algorithm will choose a set of threshold values to separate the pixel intensity into sets of desired regions. The threshold values are determined by defining the pixel values that separate the peaks of the histogram as shown in **Figure 3**. From the figure, since there are three peaks, the image pixels can be categorized into three main regions.

Figure 4(a) illustrates the original image that shows the 3 main regions (black, gray, and white) for thresholding. **Figure 4(b)** is the enhanced image and **Figure 4(c)** is the skull removed image. The purpose to remove the outer skull is to increase the sensitivity of the ICH detection algorithm by eliminating the pixels that have a similar range of density to the ICH.

Next step, the ICH in the segmented image is located using the state-of-the-art A.I-based technique, called deep neural network. Deep neural network is a type of machine learning, which consists of multiple levels of processing layers. These layers are to learn various extracting features through levels of abstraction. These enable machine learning of overly complex features from high-dimensional raw data [6]. There are several types of deep neural network, and in this project, a network called convolution neural network (CNN) is employed to detect and localize ICH on CT images [7].

CNN, or known as ConvNet, is a better option and is always considered above others. It has a deep feed-forward architecture, which contributes to its high learning efficiency in abstracting and identifying

features [8]. It is commonly used in image, voice, and text recognition and computer identification. It has a great feature of weight sharing and dimension reduction, which is the reason for its high effectiveness and efficiency, and low error rate [9].

Finally, after the ICH is located on the CT image, a rectangular shape containing the ICH is cropped. This step is important, to reduce the computational cost by performing further processing on the selected area only and avoiding any unnecessary processes. Using the same technique in skull removal, the thresholding method is applied to transform the cropped image into black and white, where the black area is the background, and the white area covered the ICH area. Thus, the ICH area can be markedly marginated and identified, and hence the surface area is measured. **Figure 5** shows the result of a CT image after (a) ICH detection and localization in a coordinate, which is then marked in (b-c) yellow box containing (d) segmented ICH using ICH binary thresholding.

Data Analysis

The performance of the developed A.I. system to calculate the accuracy of the A.I-based surface area measurement. The accuracy of the surface area was measured using the mean volumetric Dice similarity coefficients. The Dice similarity coefficients (DSC) measure the similarity between two datasets; hence the automatically segmented area was tested against the ground truth. DSC is shown in Equation (1).

$$DSC = (2 \mid X \cap Y \mid)/(\mid X \mid + \mid Y \mid) \qquad (1)$$

where |X| and |Y| are the cardinalities of the two sets (i.e., the number of elements in each set). This index equals twice the number of elements common to both sets divided by the sum of the number of elements in each set. Equation (1) also can be:

$$DSC = 2TP/(2TP + FP + FN) \qquad (2)$$

where TP is true positive, FP is false positive, and FN is false negative.

In the second stage, the statistical evaluation was performed by the sum of squared estimated of errors (SSE) between automated algorithm against ground truth, and SSE between conventional method against ground truth. The errors between these two methods were analyzed using T-test to validate the significant improvement of the developed fully automated system. The SSE calculations follow the following equation:

$$SSE = \sum_{i=1}^{n}(x_i - x)^2 \qquad (3)$$

where n is the number of observations, x_i is the value of the i-th observation, and 0 is the mean of all the observations.

RESULTS

Accuracy of Surface Area Measurement Using A.I-Based Against Conventional Method

The system performance of the ICH surface area measurement is evaluated in two statistical analyses. The first analysis is performed to evaluate the similarity index of the detected ICH area against the manually marked area by the trained radiologists. **Figure 6** shows the ICH images (a) segmented based on marking by the radiologist and (b) automated detected and segmented by the A.I. system. Whilst in **Figure 6(c)**, the green line represents the non-overlapping pixels between the two segmented images. **Table 1** shows the result of dice similarity coefficients of the detected ICH, which achieved a mean sensitivity of 0.859±0.135.

The second statistical analysis is performed to measure the significance of the developed A.I-based system as compared to the conventional method in terms of the accuracy of the measured surface area. The sum of squared estimated errors (SSE) between automated algorithm against ground truth (A.I. vs G.T.) and SSE between conventional method against ground truth (Conventional vs G.T.) was plotted as shown in **Figure 7**. The SSE for A.I. vs G.T. is median of 1.64 and standard deviation (SD) of 6.61. Meanwhile, the result for conventional vs G.T. was median of 49.62 and standard deviation (SD) of 60.09 (**Table 2**).

The t-test between both measurements is performed and has demonstrated good achievement of p-value of <0.001 (5.10 × 10^{-9}). This shows that the ICH surface area measurement using an automated AI-based system is significantly improved compared to the conventional Kothari's calculation method.

DISCUSSION

Medical error and misdiagnosis have been an inherent

part of medical practice. It can result in adverse impact on patient prognosis and recovery. It has been reported that the potential interpretation error rate in radiology is approximately 4% every year [10]. This may cause serious complications and delayed management of the patient.

There were many technologies and software developed previously to assist physicians and radiologists, in a way to reduce the margin of error. One of these is Computer Assisted Detection (CAD) in radiographic imaging and mammogram. A study has reported that CAD has an approximately 85% - 92% of accuracy in the detection of breast cancers on mammogram [11].

Artificial intelligence is another leap forward in better and developing medical technologies. Recently, many studies have undergone to create an artificial automated algorithm for detecting pathological findings in radiology and implemented it in a real hospital environment [12]. Some of these studies have also achieved approval from regulatory authorities such as the U.S. Food & Drug Administration (FDA), which considered it safe and beneficial to be used [13].

In this study, we report an A.I-based automated evaluation with accuracy comparable to that of a radiologist and conventional method of intracerebral hemorrhage on head CT. Head CT interpretation is regarded as a core skill in radiology training. The performance bar for this is accordingly high.

We demonstrate that this algorithm has achieved an adequate level of sensitivity in measuring the surface area of ICH. However, a higher rate of sensitivity may be achieved, if we used a larger number of samples to train the deep learning convolutional neural network. Future studies may be needed to further develop an enhanced version of this algorithm.

In comparison to the conventional method derived from Kothari ABC/2, this algorithm has proven to be better in accuracy with a lower error sum of squares. It shows that the measurement using this algorithm would be more precise and accurate, in comparison with the conventional and rudimentary way. This potentially gives a better insight into the patient's ICH severity, risk stratification, the cost-effectiveness of imaging tests, and better planning for optimal management.

Our future project on developing an algorithm with higher sensitivity of detection and improvement in a way of volume detection, rather than surface area, will be useful for deriving a more accurate measurement from head CT. This algorithm also can be implemented in future studies on other imaging modalities, and the detection of other types of lesions such as tumors or abscesses.

CONCLUSION

Unenhanced computed tomography of the brain is a reliable imaging technique to detect intracerebral hemorrhage. However, using the conventional and rudimentary way has a risk of delay or misdiagnosis. This A.I-based automated ICH measurement algorithm may contribute greatly to the patient's management. At the same time, it may aid and reduces the burden on the radiologist or physician.

DATA AVAILABILITY STATEMENT

The data used in this work can be requested from the corresponding author upon reasonable request.

REFERENCES

1. Caceres JA, Goldstein JN. Intracranial hemorrhage. Emergency medicine clinics of North America. 2012 Aug 1;30(3):771-94.
2. Tharek A, Muda AS, Hudi AB, Hudin AB.

INTRACRANIAL HEMORRHAGE DETECTION IN CT SCAN USING DEEP LEARNING. AJMedTech. 2022 Jan 31;2(1):1-8.

3. Bujang MA, Baharum N. A simplified guide to determination of sample size requirements for estimating the value of intraclass correlation coefficient: a review. Arch. Orofac. Sci. 2017 Jan 1;12(1).

4. Danovska MP, Alexandrova ML, Totsev NI, Gencheva II, Stoev PG. Clinical and neuroimaging studies in patients with acute spontaneous intracerebral hemorrhage. J of IMAB–Annual Proceeding Scientific Papers. 2014 Mar 28;20(2):489-94.

5. Delcourt C, Carcel C, Zheng D, Sato S, Arima H, Bhaskar S, Janin P, Salman RA, Cao Y, Zhang S, Heeley E. Comparison of ABC methods with computerized estimates of intracerebral hemorrhage volume: The INTERACT2 study. Cerebrovasc. Dis. Extra. 2019;9(3):148-54.

6. Zamani NS, Zaki WM, Huddin AB, Hussain A, Mutalib HA, Ali A. Automated pterygium detection using deep neural network. IEEE Access. 2020 Oct 13;8:191659-72.

7. Indolia S, Goswami AK, Mishra SP, Asopa P. Conceptual understanding of convolutional neural network-a deep learning approach. Procedia computer science. 2018 Jan 1;132:679-88.

8. Zhang Z. Derivation of backpropagation in convolutional neural network (cnn). University of Tennessee, Knoxville, TN. 2016 Oct 18;22:23.

9. Zhou X. Understanding the convolutional neural networks with gradient descent and backpropagation. JPCS. 2018 Apr 1;1004(1):012028)

10. Waite S, Scott J, Gale B, Fuchs T, Kolla S, Reede D. Interpretive error in radiology. AJR. 2017 Apr;208(4):739-49.

11. Brem RF, Hoffmeister JW, Zisman G, DeSimio MP, Rogers SK. A computer-aided detection system for the evaluation of breast cancer by mammographic appearance and lesion size. AJR. 2005 Mar;184(3):893-6.

12. Tharek A, Muda AS, Huddin AB, Rahim EA, Git KA, Sabri MI, Abdullah R. Padimedical: Medical Image Sharing Portal with DICOM Viewer–User Experience. International Journal of Human and Technology Interaction (IJHaTI). 2020 Oct 31;4(2):1-4.

13. Benjamens S, Dhunnoo P, Meskó B. The state of artificial intelligence-based FDA-approved medical devices and algorithms: an online database. NPJ Digit. 2020 Sep 11;3(1):1-8.

FIGURE LEGENDS
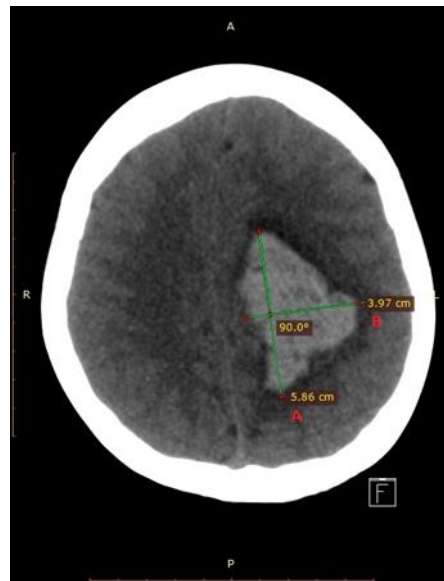
Figure 1: Conventional measurement of surface area, derived from the Kothari method. The largest diameter (A) multiplies with the largest diameter (B) 90 degrees to plane A.
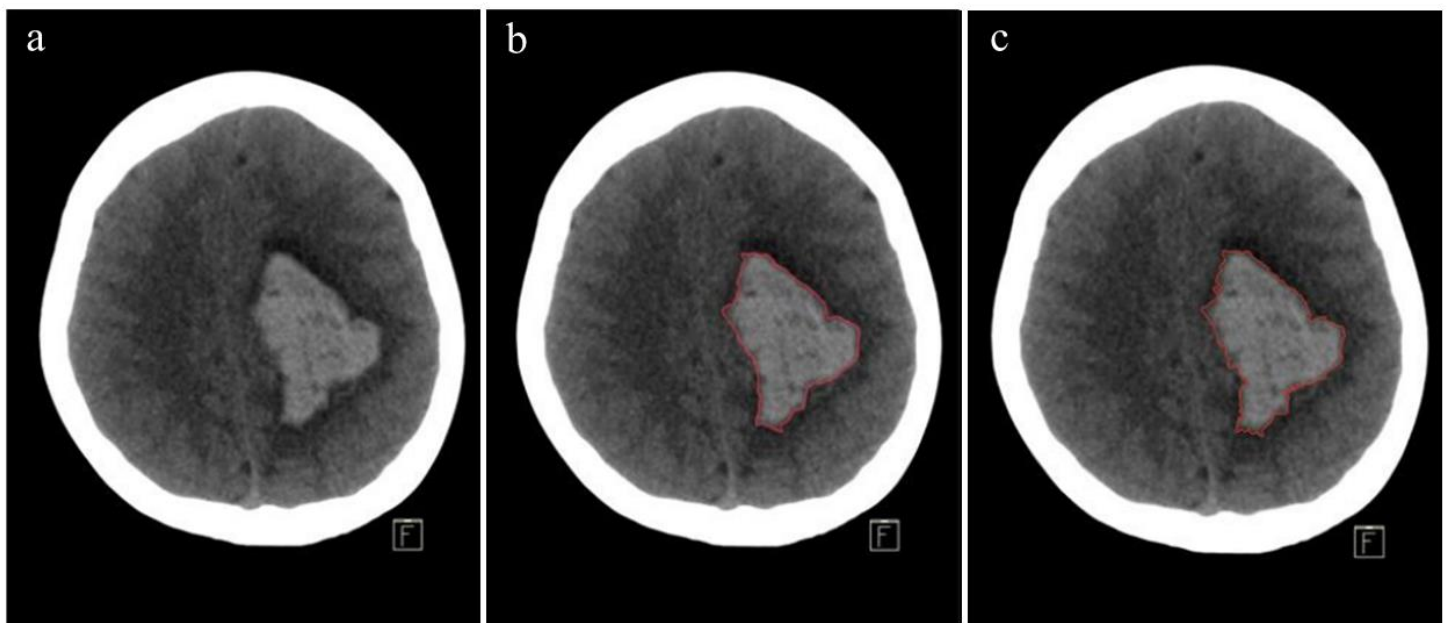
Figure 2: Manual demarcation by trained radiologists: (a) Pre-marking JPEG, (b) marking at #1 JPEG and (c) marking at #2 JPEG.
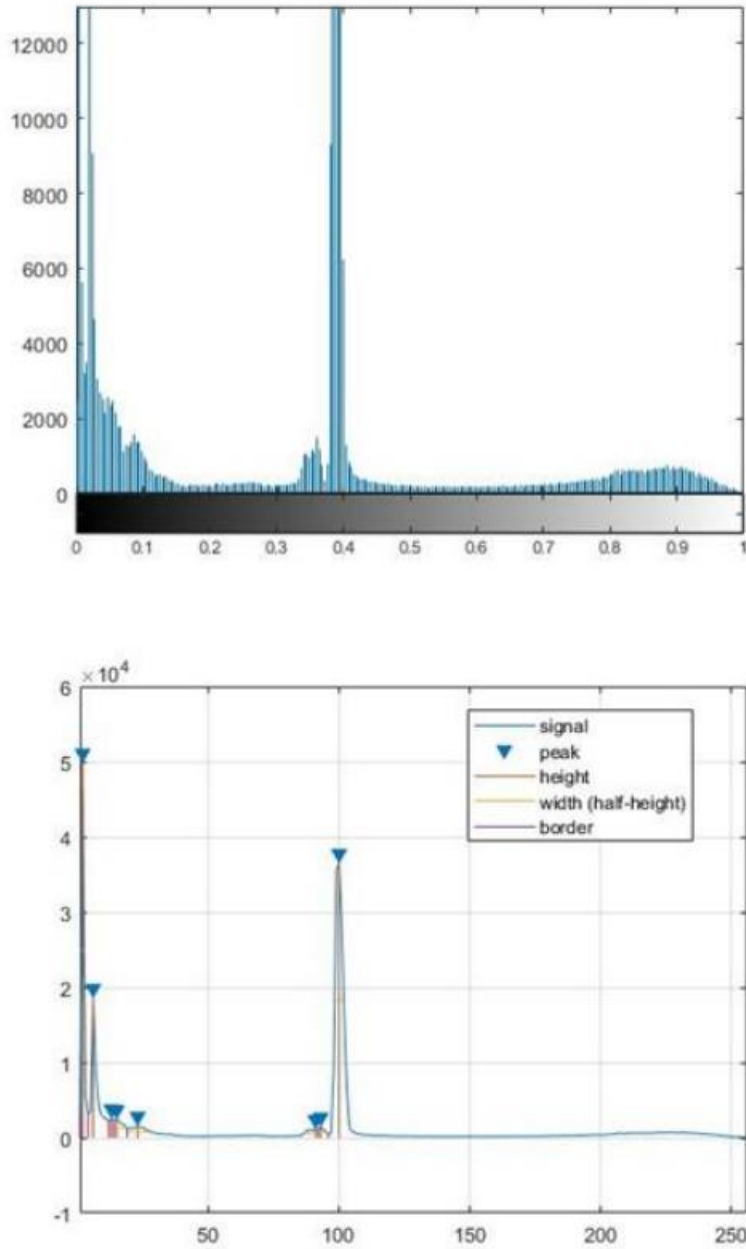
Figure 3: Histogram image of one of the data samples.
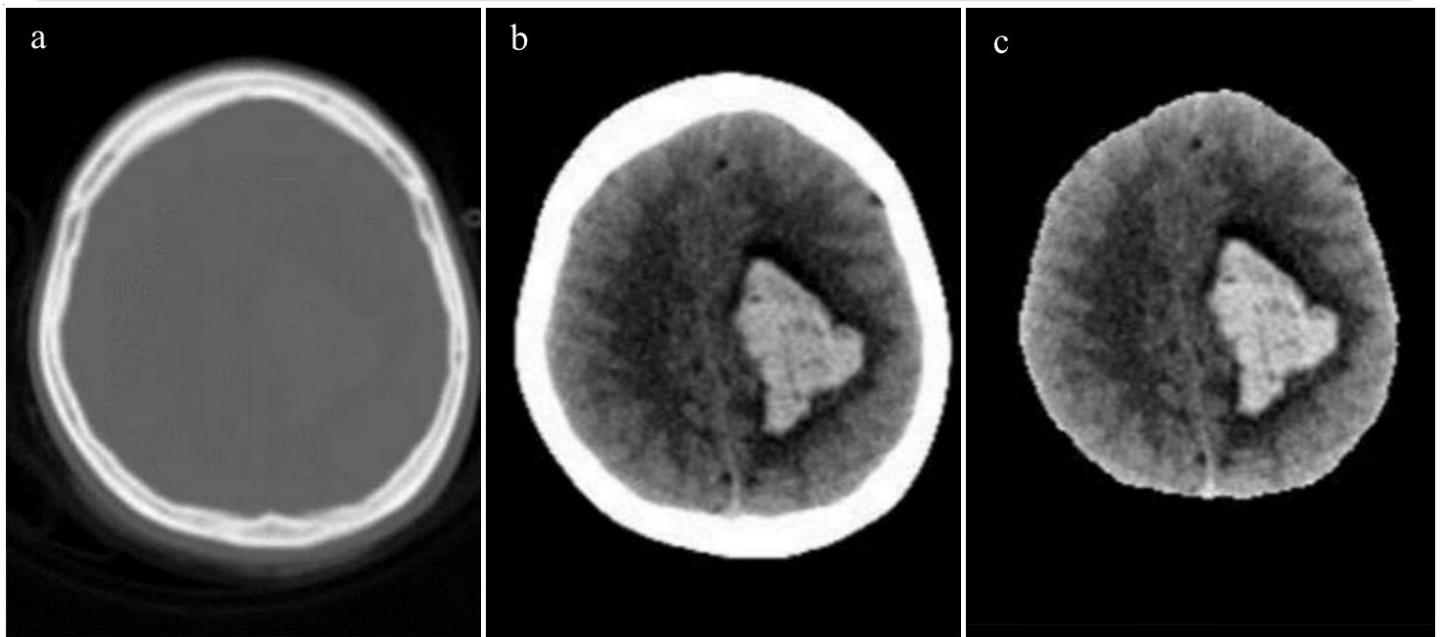
Figure 4: Segmentation using binary thresholding: (a) Original image, (b) enhanced image and (c) final skull removal image.
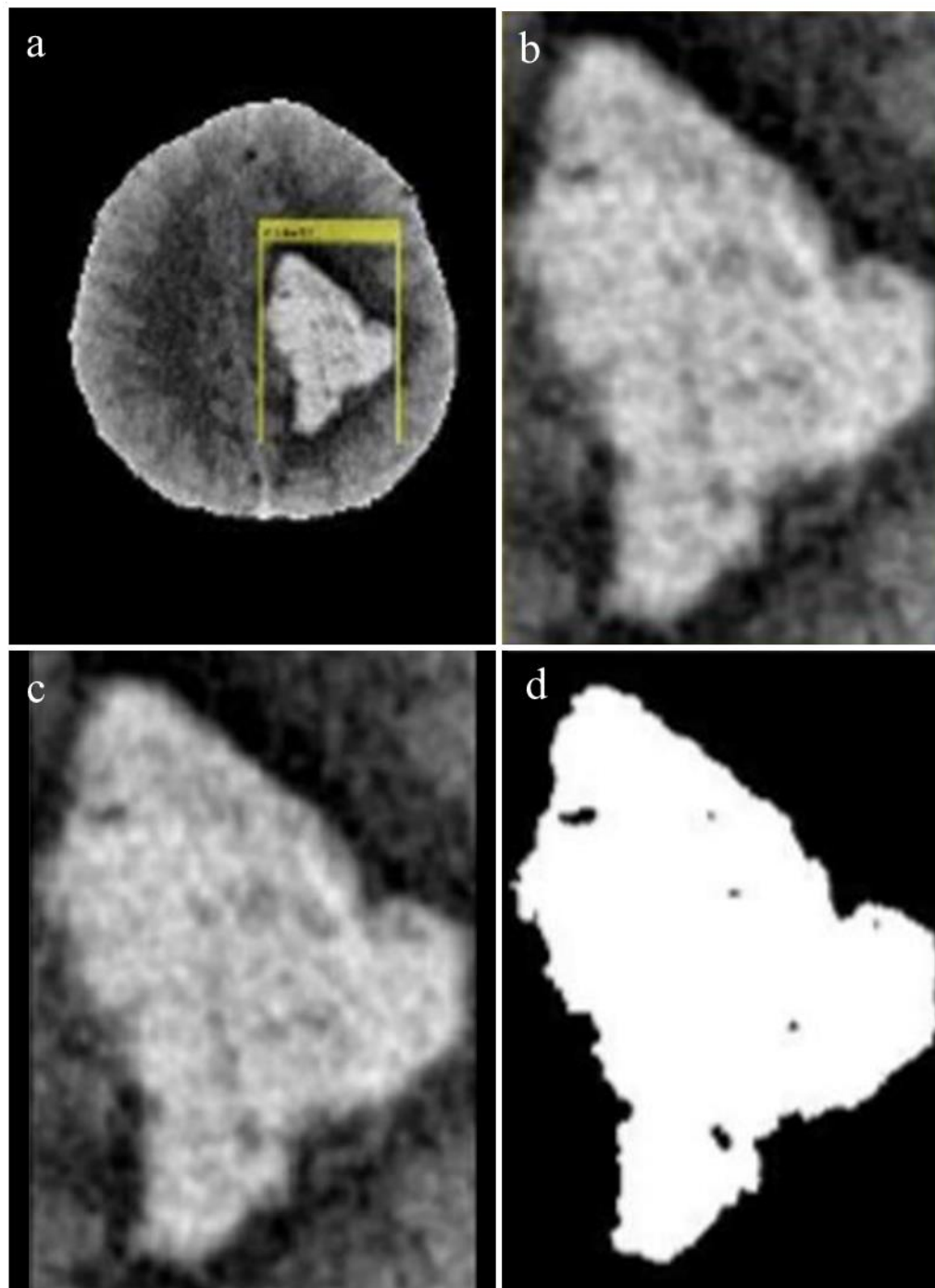
Figure 5: Automated detection and localization of ICH. (a) ICH detection and localization in a coordinate, which then is marked in (b-c) yellow box containing (d) segmented ICH using ICH binary thresholding.
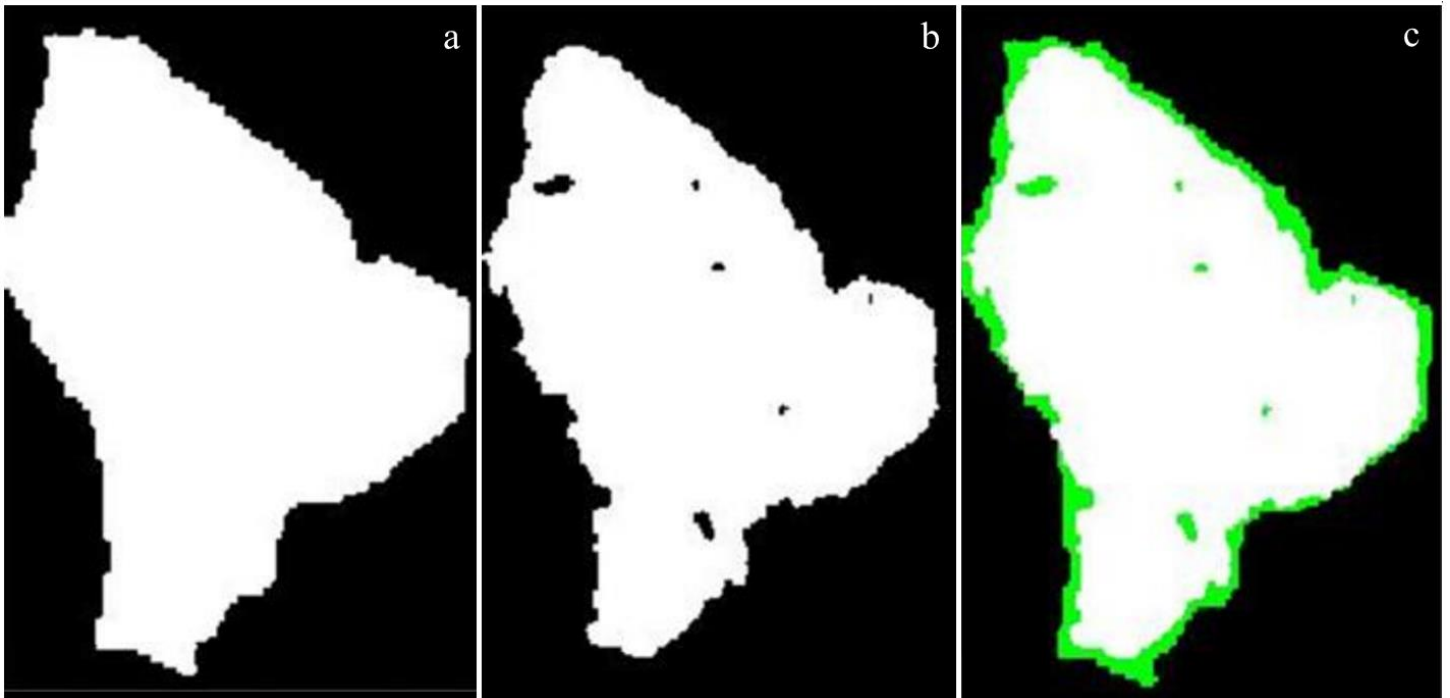
Figure 6: Evaluation of system performance based on manual demarcations and A.I-based auto-detection. (a) is marked by radiologist, (b) is auto detected and segmented and (c) demonstrates non-overlapping pixels between these two segmented images.
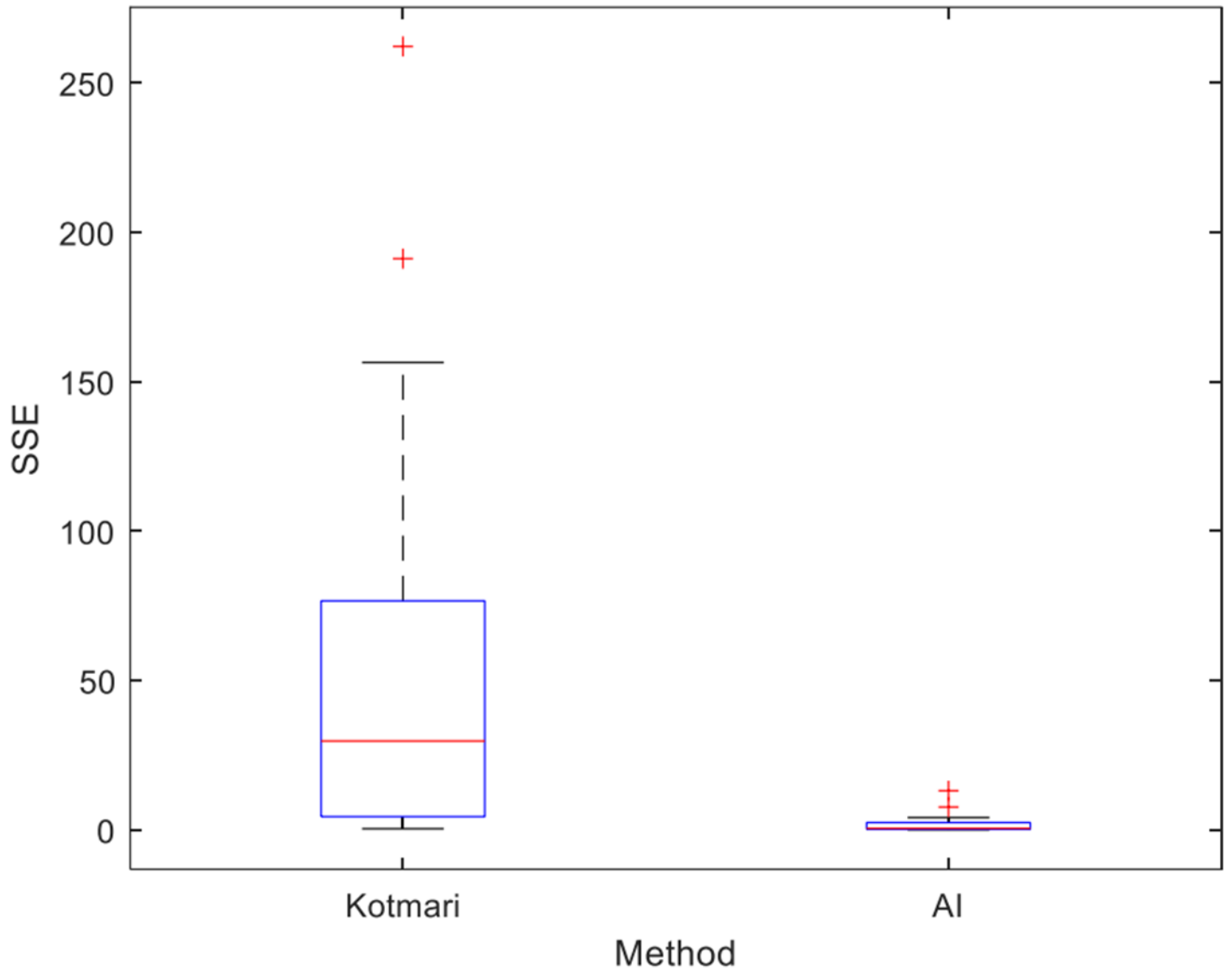
Figure 7: Boxplot showing SSE of Conventional (Kothari) vs G.T. and A.I. vs G.T.

TABLE LEGENDS

Table 1: Dice similarity coefficient of the detected ICH.

Case #	Dice Similarity Coefficient	Case #	Dice Similarity Coefficient	Case #	Dice Similarity Coefficient
011	0.932	**043**	0.888	**095**	0.717
012	0.941	**044**	0.914	**102**	0.926
013	0.936	**052**	0.821	**103**	0.889
014	0.873	**061**	0.852	**111**	0.932
015	0.870	**071**	0.816	**112**	0.869
023	0.818	**072**	0.886	**113**	0.924
024	0.786	**073**	0.884	**114**	0.915
032	0.691	**074**	0.889	**115**	0.878
033	0.857	**075**	0.904	**121**	0.773
034	0.870	**092**	0.821	**122**	0.879
035	0.853	**093**	0.790	**123**	0.844
042	0.862	**094**	0.856	**124**	0.759

Table 2: The ICH sizes using different methods and SSE of all the detected ICH.

Case #	ICH Size (cm^2)			SSE	
	Ground Truth (G.T.)	Kothari	A.I.	Kothari vs G.T.	A.I. vs G.T.
011	13.91	23.26	12.16	87.45	3.07
012	16.75	26.92	14.90	103.57	3.41
013	17.78	31.61	15.74	191.21	4.15
014	16.21	21.94	12.58	32.92	13.13
015	12.23	18.78	9.46	42.88	7.66
023	0.86	2.74	0.60	3.54	0.07
024	0.89	2.04	0.58	1.32	0.09
032	1.99	3.82	1.06	3.36	0.87
033	2.80	4.84	2.11	4.14	0.48
034	3.29	7.32	2.54	16.26	0.56
035	2.90	7.84	2.17	24.38	0.54
042	2.02	7.35	1.54	28.42	0.23
043	2.37	9.95	1.90	57.34	0.22
044	2.17	8.49	1.88	39.82	0.09
052	0.77	0.13	0.54	0.41	0.05
061	3.12	4.85	2.33	2.99	0.63
071	4.47	10.04	3.09	31.10	1.89
072	7.83	13.76	6.26	35.11	2.49
073	8.94	14.85	7.11	34.93	3.35
074	9.95	14.50	7.98	20.67	3.88
075	9.13	12.37	7.55	10.53	2.47
092	1.80	3.71	1.27	3.64	0.28
093	1.74	5.01	1.14	10.68	0.36
094	1.28	3.78	1.03	6.26	0.06
095	0.76	2.94	0.43	4.76	0.11
102	1.29	2.69	1.14	1.94	0.02
103	1.18	2.39	0.95	1.46	0.05
111	5.75	21.94	5.08	262.23	0.44
112	5.59	18.09	4.31	156.45	1.63
113	4.54	16.01	3.92	131.37	0.39
114	3.85	12.94	3.27	82.68	0.34
115	3.11	12.25	2.45	83.51	0.44
121	2.62	7.72	1.66	26.02	0.91
123	3.55	11.13	2.81	57.51	0.54
124	4.27	14.97	3.13	114.65	1.30
125	4.40	12.80	2.71	70.63	2.87

THE MRI FEATURES IN DIAGNOSING TUMEFACTIVE DEMYELINATING LESION

See Yun Foo[1], Nurul Hafidzah Rahim[2], Aida Widure Mustapha Mohd Mustapha[*1], Noraini Rose Mohd Zaini[2]

[1] Department of Radiology, Hospital Canselor Tuanku Muhriz, Universiti Kebangsaan Malaysia, Cheras, Malaysia
[2] Department of Radiology, Hospital Kuala Lumpur, Kementerian Kesihatan Malaysia, Kuala Lumpur, Malaysia

*Corresponding author:
Aida Widure Mustapha Mohd Mustapha, Department of Radiology, Hospital Canselor Tuanku Muhriz, Universiti Kebangsaan Malaysia, Cheras, Malaysia.
Email: aida.widure.mustapha@ppukm.ukm.edu.my

ABSTRACT

Background: A demyelinating lesion can present as a space occupying lesion in Magnetic Resonance Imaging (MRI) brain. Lesions that have diameter greater than 2 cm is referred as tumefactive demyelinating lesion. These lesions can mimic a brain tumor, namely glioma or primary central nervous system lymphoma.

Case presentation: We present two female patients over 30 years old who presented with limb weakness. Their MRI demonstrated typical appearance of a solitary, incomplete rim enhancing lesion that involved the subcortical white matter with minimal mass effect. Also, the rim of enhancement opened to the grey matter. Due to their typical appearance, biopsy was not performed. The lesions in both patients reduced in size upon follow up after treatment commencement and currently recovering.

Conclusion: In this case report, we focus on discussing the MRI features of tumefactive demyelinating lesion and its main differentials, which are central nervous system lymphoma (CNSL) and glioma.

Keywords: Magnetic Resonance Imaging (MRI); Tumefactive demyelinating lesion (TDL); Open ring enhancement

INTRODUCTION

A demyelinating lesion can present as a space occupying lesion mimicking brain tumor (1). With a diameter greater than 2 cm, it is referred to as a tumefactive demyelinating lesion (TDL), which may have variable presentation. In this case report, we present two cases of TDL and discuss about the findings as well as differential diagnosis.

CASE PRESENTATION

Case 1

Madam B, 44 years old female with underlying diabetes mellitus, and previously activities of daily living (ADL) independent. She presented with aphasia, difficulty reading and expressing word for 5 months and progressive right sided body weakness for 2 months. The body weakness worsened and she became wheelchair bound. No history of fever, loss of appetite or weight loss. On examination, there was right sided homonymous hemianopia, reduced tone, power and sensation of the right upper and lower limbs. After thorough neurological examination, the provisional diagnosis was left parietal lobe syndrome with pyramidal sign; TRO inflammation / demyelinating syndrome. Her initial brain computed

tomography (CT) scan reported lesion in the left parietal lobe. Her blood investigation and cerebral spinal fluid (CSF) study negative for infection. White cell count and inflammatory marker were not elevated and her CSF study is normal. Anti-Aquaporin 4 antibody is negative. Magnetic resonance imaging (MRI) of her brain showed ill-defined left parietal lobe white matter lesion measuring 4.5 cm in widest dimension, which demonstrated hypointensity on T1W, high signal intensity on T2W images with heterogenicity within and incomplete rim enhancement. No significant perilesional edema or mass effect detected. The overall features were suggestive of TDL with differential diagnosis of primary brain tumor. A repeated MRI brain with added advance MRI sequences which are magnetic resonance spectroscopy (MRS) was then performed. The findings show significant raised Choline and reduced NAA particularly at the center of the lesion which suggests neuronal loss. This helped in confirming that the lesion is demyelinating lesion. She was treated with methylprednisolone 1 g OD for 5 days, followed by 5 sessions of plasma exchange and is currently on two monthly intravenous (IV) cyclophosphamide 500 mg while awaiting for social welfare support for IV Rituximab. Her symptoms improved following treatment and two follow up MRI brain showed smaller size of the lesion and resolution of the incomplete rim enhancement (**Figure 1**).

Case 2

Madam H, 38 years old female, no known medical illness, previously ADL independent. She complained of progressive right sided upper, then lower limb weakness. Subsequently, she required wheelchair for ambulation. On examination, there were increased tone and reflex and reduced power of the right upper and lower limbs. Sensations of her limbs were intact. Her blood investigation and CSF study does not favor infection. White cell count and inflammatory marker were not elevated and her CSF study is normal. Anti-Aquaporin 4 antibody is negative. CT brain and MRI brain showed left parietal intra-axial cystic lesion. The provisional differential diagnosis was neuroglial cyst and atypical supratentorial cystic astrocytoma. Repeat MRI brain showed left frontoparietal lesion

measuring 4.5 cm in widest dimension. The lesion involved the subcortical white matter and cortex with minimal mass effect. The lesion had low signal on T1W images and high signal intensity on T2W images with peripheral incomplete rim enhancement. The overall findings were suggestive of TDL. She was treated with IV methylprednisolone 1 g for five days subsequently 1 session of plasma exchange and has completed 4th cycle of IV rituximab. Her symptoms improved after the treatment. Two follow up MRI brain showed reduction in size of the lesion and resolution of the incomplete rim enhancement (**Figure 2**).

DISCUSSION

TDL is a lesion with usual size greater than 2 cm diameter (2, 3). Solitary TDL is the most common initial MRI findings (3). It may exhibit mass effect, with or without perilesional edema and with or without contrast enhancement (1, 3). Subcortical white matter is commonly involved followed by the periventricular white matter and brainstem (1). The common location of TDL is supratentorial region especially frontal and parietal region (4). Smaller demyelinating lesion in between 0.5 to 2 cm may also demonstrate similar imaging findings (5).

It is a female predominant condition with female to male ratio of 2.3:1 (1, 6). The mean age of onset is in the third decade (3, 6, 7). In our case, both of the patients are female aged over thirty years old.

The clinical presentation of TDL can be variable. The majority is pyramidal involvement such as limb weakness, hemiparesis or hemiplegia (3, 8). Other involvement includes sensory, brainstem, cerebellar, optic neuritis, visual field defects, dysfunction of the bowel or bladder, sexual dysfunction, acute cognitive changes, global aphasia, diplopia, and epileptic seizures (3, 8). Both of our patients had limb weakness. One of them initially presented with aphasia.

21% of patients with TDL developed classical multiple sclerosis (MS) during follow-up (3). In our cases, both the patients had brain and whole spine MRI during their follow up but did not show new brain or spinal cord lesions.

As TDL is one of the mimicker of a CNS neoplasm such as glioma and CNS lymphoma (CNSL), there are few MRI features that help to differentiate them. Most of the TDL and CNSL

demonstrate hypointensity or mixed signal intensity relative to white matter on T1W images. Both TDL and CNSL also demonstrate hyperintensity or mixed signal intensity compared to grey matter on T2W images (9). In our cases, the lesions demonstrated T1W hypointensity as compared to white matter and T2W hyperintensity as compared to grey matter. On post contrast study, majority of TDL demonstrate incomplete rim enhancement as compared to CNSL and glioma (7, 9). Some authors commented that the enhancement is seen in active demyelination (10). The incomplete portion of the rim opens to the grey matter (2, 11). The part of the rim enhancement in the white matter represents the leading edge of demyelination while the non-enhancing center represents chronic phase (2). In both of our cases, the incomplete rim enhancement opened to the grey matter which matched the characteristic MRI findings of demyelination.

There are a few MRI features which are more commonly seen in TDL as compared to CNS glioma. One of it is area of T2W hyperintensity that does not show enhancement on post gadolinium image (12). In this case report, the T2W high signal intensity areas of both patients did not demonstrate enhancement on post gadolinium study.

Other than conventional MRI, MR perfusion is an advanced MRI technique that helps to differentiate TDL from other CNS neoplasm with similar conventional MRI features. In a study conducted by Cha et al, all TDLs had relative cerebral blood volume (rCBV) of less than 2 ml/100 g. Comparing with CNS neoplasm, there is statistically significant in the difference in mean rCBV between both TDL and CNS neoplasm in which higher rCBV is expected in neoplasm due to neovascularity (4, 13). In our case reports, MR perfusion was performed on the first case and her rCBV value is less than 2 ml/100 g which is not suggestive of CNS neoplasm.

With the emerging used of advanced MRI techniques, apparent diffusion coefficient (ADC) value and Magnetic Resonance Spectroscopy (MRS) were also used to differentiate TDL and CNS neoplasm.

The center of TDL which has myelin destruction and edema changes will have high ADC value while the periphery enhancing region of TDL has low ADC value. A threshold of 0.556×10^{-3} mm^2/s has 81.3% sensitivity and 88.9% specificity in distinguishing TDL from primary CNS neoplasm (14). Study by Lu et al stated significant difference seen between PCNSL and TDL. The minimum value of ADC histogram (ADCmin) of TDL is $684 \pm 101 \times 10^{-6}$ mm^2/s while the ADCmin of PCNSL is lower, which is $563 \pm 90 \times 10^{-6}$ mm^2/s (14).

TDL will demonstrate increased choline (CHO) peak and decreased N-acetyl aspartate (NAA) peak with increased Cho/NAA ratio. A Cho/NAA ratio of greater than 1.72 or 1.73 favors high grade CNS neoplasm. Therefore, in adjunct to the findings in conventional MRI, this helps increase the confident in diagnosing TDL. Lactate peak and glutamate-glutamine peak may also see in TDL (4, 15).

Correlating the CT features of the TDL with the MR feature also plays a role. The enhancing component of TDL in MRI appears hypodense on CT scan. This finding is highly specific. Meanwhile, the enhancing component on MRI in CNSL and glioma mostly demonstrate either isodense or hyperdense on CT scan (9, 12). Unfortunately, the CT images of the patients were not available for correlation. The common sites of metastases are lungs, liver and bones (3). In the head and neck region, the nose and the paranasal sinuses is the commonest site for metastasis of RCC (3). However, primary tumor of the nasal and paranasal regions is still the commonest compared to metastatic disease.

CONCLUSION
In conclusion, although differentiating TDL from CNS tumor can be challenging for the reporting radiologist. However, the typical imaging features in TDL can increase confidence in diagnosing it. In these cases, the characteristic open rim enhancement where the enhancing rim signify the leading edge of demyelination and open to grey matter with supporting finding of T2W hyperintensity which does not enhance in post contrast study point toward TDL rather than other diagnosis such as CNSL and glioma. Other than conventional MRI findings, advanced MRI techniques such as MR perfusion and MRS serve as great adjuncts to the diagnosis of TDL. Together with the experience of the reporting radiologist, both patients are diagnosed with TDL in their initial MRI in our center. Biopsies were avoided and both patients responded to treatment and currently on regular follow up.

STATEMENT OF ETHICS
Written informed consent was obtained from the patients for publication of this case and any accompanying images.

ACKNOWLEDGEMENTS

CONFLICT OF INTEREST
The authors declare that they have no conflict of interest.

FUNDING

DATA AVAILABILITY STATEMENT
No additional data than the one presented in this article was used

REFERENCES
1. Jeong IH, Kim SH, Hyun JW, Joung A, Cho HJ, Kim HJ. Tumefactive demyelinating lesions as a first clinical event: Clinical, imaging, and follow-up observations. J Neurol Sci. 2015 Nov 15;358(1-2):118-24.
2. Given CA 2nd, Stevens BS, Lee C. The MRI appearance of tumefactive demyelinating lesions. AJR Am J Roentgenol. 2004 Jan;182(1):195-9.
3. Vakrakou AG, Tzanetakos D, Evangelopoulos M-E, Argyrakos T, Tzartos JS, Anagnostouli M, et al. Clinico-radiologic features and therapeutic strategies in tumefactive demyelination: a retrospective analysis of 50 consecutive cases. Therapeutic Advances in Neurological Disorders. 2021;14:18.
4. Kilic AK, Kurne AT, Oguz KK, Soylemezoglu F, Karabudak R. Mass lesions in the brain: tumor or multiple sclerosis? Clinical and imaging characteristics and course from a single reference center. Turk Neurosurg. 2013;23(6):728-35.
5. Patriarca L, Torlone S, Ferrari F, Di Carmine C, Totaro R, di Cesare E, Splendiani A. Is size an essential criterion to define tumefactive plaque? MR features and clinical correlation in multiple sclerosis. Neuroradiol J. 2016 Oct;29(5):384-9.
6. Altintas A, Petek B, Isik N, Terzi M, Bolukbasi F, Tavsanli M, Saip S, Boz C, Aydin T, Arici-Duz O, Ozer F, Siva A. Clinical and radiological characteristics of tumefactive demyelinating lesions: follow-up study. Mult Scler. 2012 Oct;18(10):1448-53.
7. Mabray MC, Cohen BA, Villanueva-Meyer JE, Valles FE, Barajas RF, Rubenstein JL, Cha S. Performance of Apparent Diffusion Coefficient Values and Conventional MRI Features in Differentiating Tumefactive Demyelinating Lesions From Primary Brain Neoplasms. AJR Am J Roentgenol. 2015 Nov;205(5):1075-85.
8. Balloy G, Pelletier J, Suchet L, Lebrun C, Cohen M, Vermersch P, Zephir H, Duhin E, Gout O, Deschamps R, Le Page E, Edan G, Labauge P, Carra-Dallieres C, Rumbach L, Berger E, Lejeune P, Devos P, N'Kendjuo JB, Coustans M, Auffray-Calvier E, Daumas-Duport B, Michel L, Lefrere F, Laplaud DA, Brosset C, Derkinderen P, de Seze J, Wiertlewski S; Société Francophone de la Sclérose en Plaques. Inaugural tumor-like multiple sclerosis: clinical presentation and medium-term outcome in 87 patients. J Neurol. 2018 Oct;265(10):2251-2259.
9. Lin X, Yu WY, Liauw L, Chander RJ, Soon WE, Lee HY, Tan K. Clinicoradiologic features distinguish tumefactive multiple sclerosis from CNS neoplasms. Neurol Clin Pract. 2017 Feb;7(1):53-64.
10. Smirniotopoulos JG, Murphy FM, Rushing EJ, Rees JH, Schroeder JW. Patterns of contrast enhancement in the brain and meninges. Radiographics. 2007 Mar-Apr;27(2):525-51.
11. Masdeu JC, Quinto C, Olivera C, Tenner M, Leslie D, Visintainer P. Open-ring imaging sign: highly specific for atypical brain demyelination. Neurology. 2000 Apr 11;54(7):1427-33.
12. Kim DS, Na DG, Kim KH, Kim JH, Kim E, Yun BL, Chang KH. Distinguishing tumefactive demyelinating lesions from glioma or central nervous system lymphoma:

added value of unenhanced CT compared with conventional contrast-enhanced MR imaging. Radiology. 2009 May;251(2):467-75.

13. Cha S, Pierce S, Knopp EA, Johnson G, Yang C, Ton A, Litt AW, Zagzag D. Dynamic contrast-enhanced T2*-weighted MR imaging of tumefactive demyelinating lesions. AJNR Am J Neuroradiol. 2001 Jun-Jul;22(6):1109-16.

14. Lu SS, Kim SJ, Kim N, Kim HS, Choi CG, Lim YM. Histogram analysis of apparent diffusion coefficient maps for differentiating primary CNS lymphomas from tumefactive demyelinating lesions. AJR Am J Roentgenol. 2015 Apr;204(4):827-34.

15. Nakayama M, Naganawa S, Ouyang M, Jones KA, Kim J, Capizzano AA, Moritani T. A Review of Clinical and Imaging Findings in Tumefactive Demyelination. AJR Am J Roentgenol. 2021 May 19:1-12.

FIGURE LEGENDS
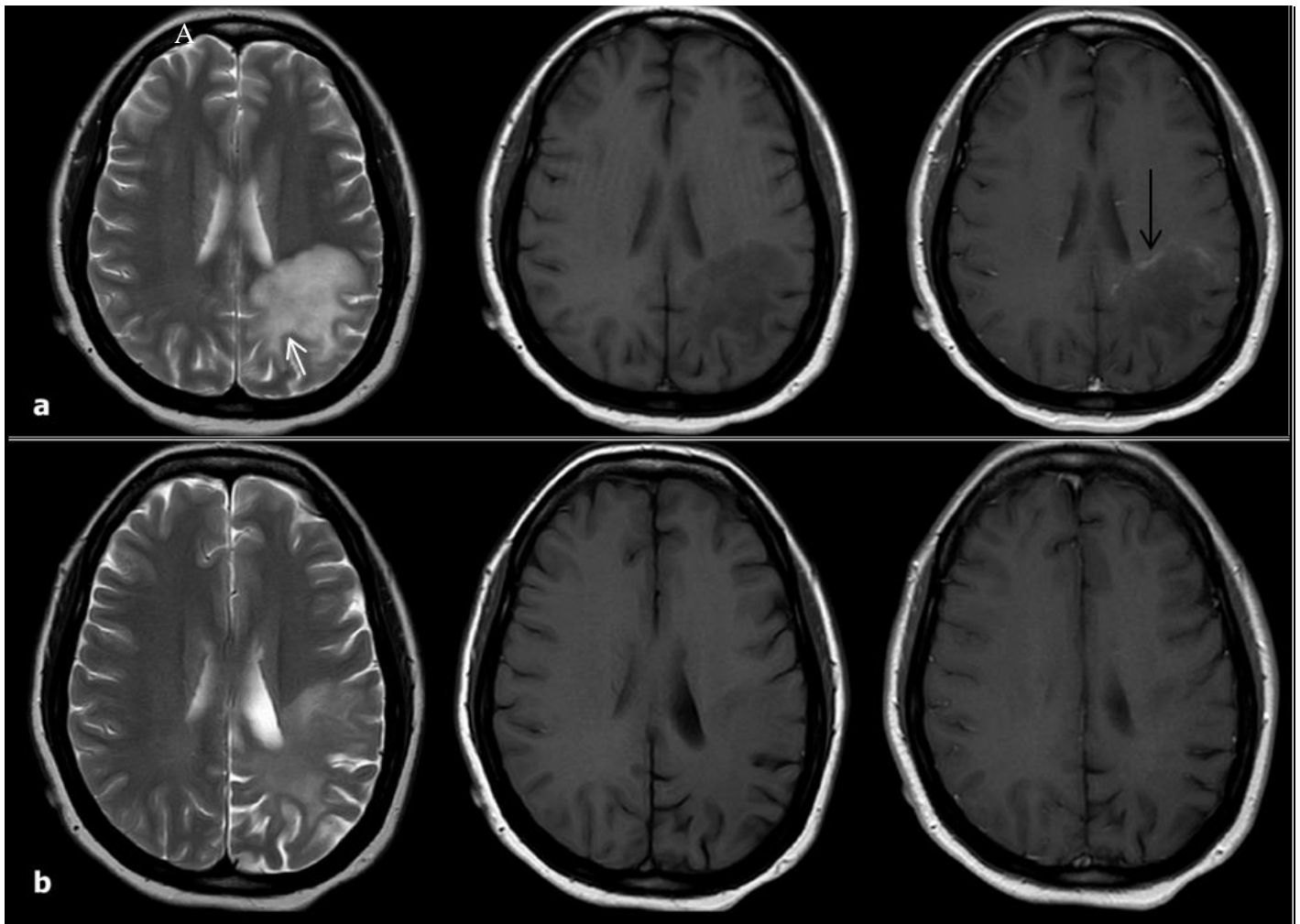
Figure 1: MRI brain of case 1. (a) Initial MRI with left parietal lobe white matter lesion extending to subcortical U-fibers that shows high signal intensity on T2W (white arrow), low signal intensity on T1W and incomplete rim enhancement in post-gadolinium study (black arrow). Note that the high signal intensity area on T2W is not enhancing in post-gadolinium study. (b) Latest MRI done 5 months apart shows resolving lesion with no enhancement.
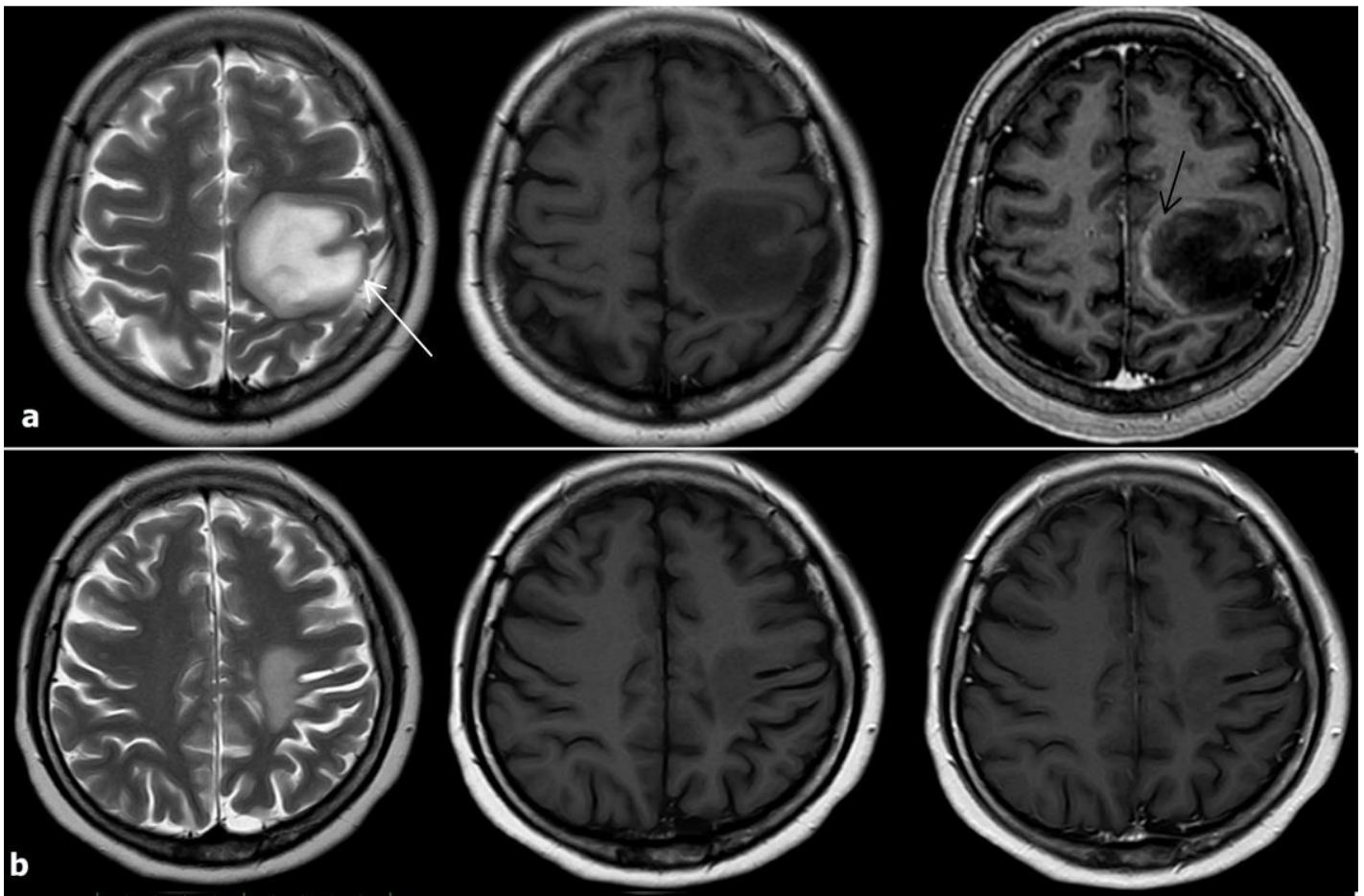
Figure 2: MRI brain of case 2. (a) Initial MRI shows left frontoparietal lobe lesion involving the subcortical white matter and cortex demonstrating high signal intensity on T2W (white arrow), low signal intensity on T1W and incomplete rim enhancement on post-gadolinium study (black arrow). The high signal intensity area on T2W does not enhance in post-gadolinium study. (b) Latest MRI in 4 months apart shows significantly smaller lesion with resolution of enhancement.

RIGHT CORONARY ARTERY ORIGINATING FROM LEFT ANTERIOR DESCENDING ARTERY: A RARE VARIANT OF SINGLE CORONARY ARTERY DETECTED ON CT CORONARY ANGIOGRAPHY

Mohd Hafizuddin Husin[*1], Ahmad Aizuddin Mohamad Jamali[1], Mohd Azaad A Hamid[1], Khairulanuar Saad[2]

[1]Department of Radiology, School of Medical Sciences, Universiti Sains Malaysia, Kubang Kerian, Malaysia
[2]Diagnostic Imaging Department, Hospital Raja Perempuan Zainab II, Kota Bharu, Malaysia

*Corresponding author:
Mohd Hafizuddin Husin, School of Medical Sciences, Universiti Sains Malaysia, Kubang Kerian, Malaysia
Email: mohafizmh@usm.my

ABSTRACT

Background: A single coronary artery (SCA) is a rare anomaly encountered using conventional coronary angiography. A right coronary artery (RCA) originating from a left anterior descending artery (LAD) is a rare subtype of SCA. Only a few cases are described in published literature.

Case presentation: We described this anomaly in a 55-year-old male who presented with angina pectoris. The anomalous RCA was suspected by conventional coronary angiogram and was confirmed by computed tomography (CT) coronary angiography. Using CT, we demonstrated the course of the abnormal vessel and its relation to the main vessel. We also detected the presence of plaque, which caused luminal stenosis of the proximal LAD, which may cause global ischaemia.

Conclusion: We concluded that although conventional coronary angiography is an important diagnostic method, new non-invasive methods such as CT coronary angiography can be a better screening tool to detect and characterise coronary anomalies.

Keywords: Anomalous right coronary artery; Single coronary artery; CT coronary angiography

INTRODUCTION

Single coronary artery (SCA) is a rare anomaly encountered only in 0.031% of the population. The right coronary artery (RCA) originates from the left anterior descending artery (LAD), an extremely rare SCA variant. Only about 30 cases of the anomalies are reported in previous literature (1-3). Until the development of multidetector computed tomography, coronary artery anomalies were mainly evaluated by invasive conventional coronary angiography (4, 5). We describe a case of a very rare variant of SCA in which an anomalous RCA arises from the mid-LAD. This anomaly was detected during a routine coronary angiogram and then confirmed on computed tomography (CT) coronary angiography.

CASE PRESENTATION

A 54-year-old Malay ex-smoker with underlying type

2 diabetes mellitus presented to the emergency department with a one-day history of dull aching left-sided chest pain, which was aggravated by physical activity. Upon arrival, he was hemodynamically stable. An electrocardiogram (ECG) revealed atrial fibrillation with a heart rate of 110. No acute ischaemic changes were present. An echo showed good left ventricular function with an ejection fraction of 70%. A serial blood test showed raised creatine kinase-MB (CKMB). He was treated as angina pectoris with atrial fibrillation, and a coronary angiogram was scheduled.

Coronary angiography showed a single coronary ostium with the left main coronary artery bifurcates to the LAD and the left circumflex artery (LCX) (**Supplementary material 1**). There was a mild proximal LAD disease. Multiple aortic root injections confirmed the absence of a conventional RCA originating from the anterior coronary sinus.

CT coronary angiography showed a single left main coronary artery (LMCA) originating from the left coronary cusp. The LMCA demonstrates a normal course and divides into the LAD and LCX. The LAD courses inferiorly within the anterior interventricular groove. There is mild stenosis at the proximal aspect of the left LAD – CAD-RADS 2 with a mild plaque burden (P1) according to the 2022 Coronary Artery Disease – Reporting and Data System (CAD-RADS 2.0)(**Figure 1**). The anomalous RCA originates from the mid-portion of LAD. This RCA courses laterally and anteriorly to the pulmonary trunk. It runs into the right atrioventricular groove and gives rise to a posterior descending artery (PDA) distally, indicating a right dominant system (**Figure 2, Supplementary material 2**).

DISCUSSION

Coronary artery anomalies can be defined as a coronary pattern or feature encountered in less than 1% of the population (1). SCA is a rare coronary anomaly in which the RCA and the LMCA arise from a single aortic sinus. It was first described in 1903, and several cases of SCA have been reported. In a recent retrospective study by Turkmen et al. that included 215140 patients undergoing coronary angiography, only 67 patients were detected to have this anomaly (0.031%) (1, 3).

The origin of an anomalous RCA may be from the left sinus of Valsalva, posterior sinus of Valsalva, ascending aorta, pulmonary artery, left ventricle, LMCA, LCX or LAD. RCA arising from the LAD is an extremely rare SCA variant occurring in approximately 0.024%-0.066% of the general population undergoing coronary angiography (2). Several authors have attempted to classify coronary artery anomalies. However, no single classification is widely accepted. In a recent review, Villa et al. suggest a classification based on anatomical features. The anomalies of origin are divided into anomalies of origin from the pulmonary artery and anomalies of origin from the aorta. SCA falls into anomalies of origin from the aorta, further classified into SCA origin from the left sinus of Valsalva and SCA origin from the right sinus of Valsalva (1). The anomaly encountered in our patient was not described in this classification. The closest category that our patients' coronary anatomy represented was that of the LIIA anomaly.

Coronary angiography has traditionally been the gold standard in detecting coronary artery disease and coronary artery anomalies. A non-invasive method such as CT coronary angiography produces comparable results. It has been shown that CTA coronary sensitivity in visualising abnormal vessels is 100% (4).

CTA coronary has multiple benefits besides non-invasiveness, including providing 3D information, high spatial resolution, and rapid examination time. It is superior in identifying the course of potentially malignant course – inter-arterial, in which the coronary artery passes between the aorta and the main pulmonary artery. In our case, the anomalous RCA has a benign course as it passes anterior to the pulmonary artery. It also can detect other high-risk anatomic features such as slit-like ostium, proximal narrowing of the vessel, intra-mural course and acute take-off angle. The prevalence of coronary anomalies is also higher on CTA coronary than on conventional coronary angiograms (4-6).

Because of its invasiveness, radiation exposure, and inability to characterise non-coronary cardiac anatomy, conventional coronary angiography in coronary artery anomalies should only be used to complement non-invasive imaging (6).

CONCLUSION

Anomalous RCA originating from the LAD is a rare

entity. We report an interesting case of the RCA originating from the mid-LAD, which was confirmed using CT coronary angiography. When combined with other non-invasive imaging such as cardiac magnetic resonance imaging or nuclear and hybrid imaging to detect high-risk physiologic consequences of coronary anomalies, CT coronary angiography is a better choice than conventional angiography as a screening tool.

STATEMENT OF ETHICS
Informed consent was obtained from the patients to publish the case report and the accompanying images.

CONFLICT OF INTEREST
The authors have no known conflict of interest to disclose.

FUNDING
The authors received no funding from any party for this scientific work.

DATA AVAILABILITY STATEMENT
No additional data than the one presented in this article was used

REFERENCES
1. Villa AD, Sammut E, Nair A, Rajani R, Bonamini R, Chiribiri A. Coronary artery anomalies overview: The normal and the abnormal. World J. Radiol. 2016 Jun;8(6):537.
2. Yurtdas M, Gulen O. Anomalous origin of the right coronary artery from the left anterior descending artery: review of the literature. Cardiol. J. 2012 Mar;19(2):122-129.
3. Turkmen S, Yolcu M, Sertcelik A, Ipek E, Dokumaci B, Batyraliev T. Single coronary artery incidence in 215,140 patients undergoing coronary angiography. Folia Morphol. 2014 Nov;73(4):469-474.
4. Erol C, Seker M. Coronary Artery Anomalies: The Prevalence of Origination, Course, and Termination Anomalies of Coronary Arteries Detected by 64-Detector Computed Tomography Coronary Angiography. JCAT. 2011 Sep;35(5):618-624.
5. Ghadri JR, Kazakauskaite E, Braunschweig S, Burger IA, Frank M, Fiechter M, et al. Congenital coronary anomalies detected by coronary computed tomography compared to invasive coronary angiography. BMC Cardiovasc. Disord. 2014 Dec;14(1):81.
6. Grani C, Buechel RR, Kaufmann PA, Kwong RY. Multimodality Imaging in Individuals With Anomalous Coronary Arteries. JACC Cardiovasc. Imaging. 2017;10(4):471-481.

FIGURE LEGENDS
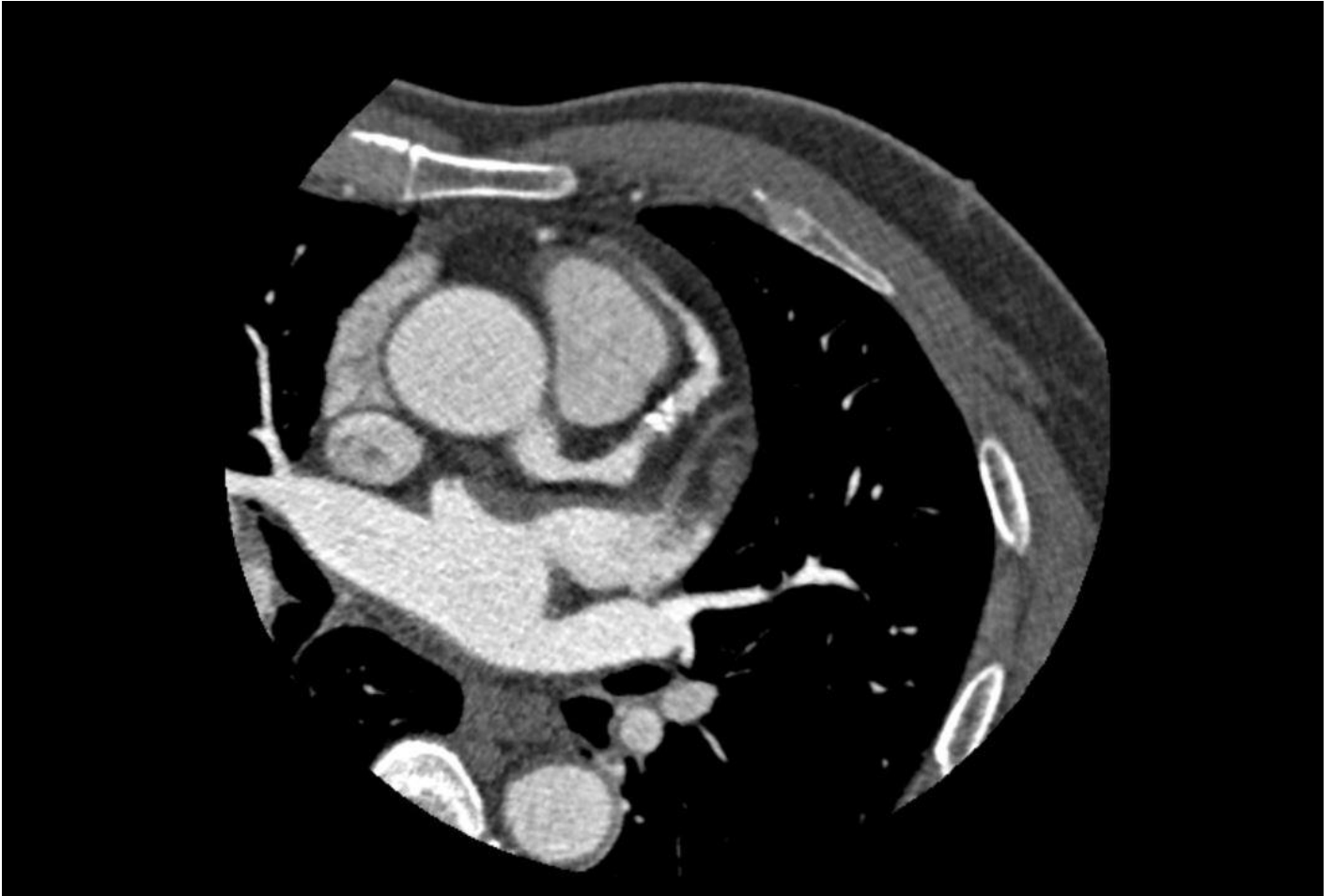
Figure 1: Mild coronary plaque (P1) within the proximal aspect of LAD with 25-49% stenosis (CAD-RADS 2).
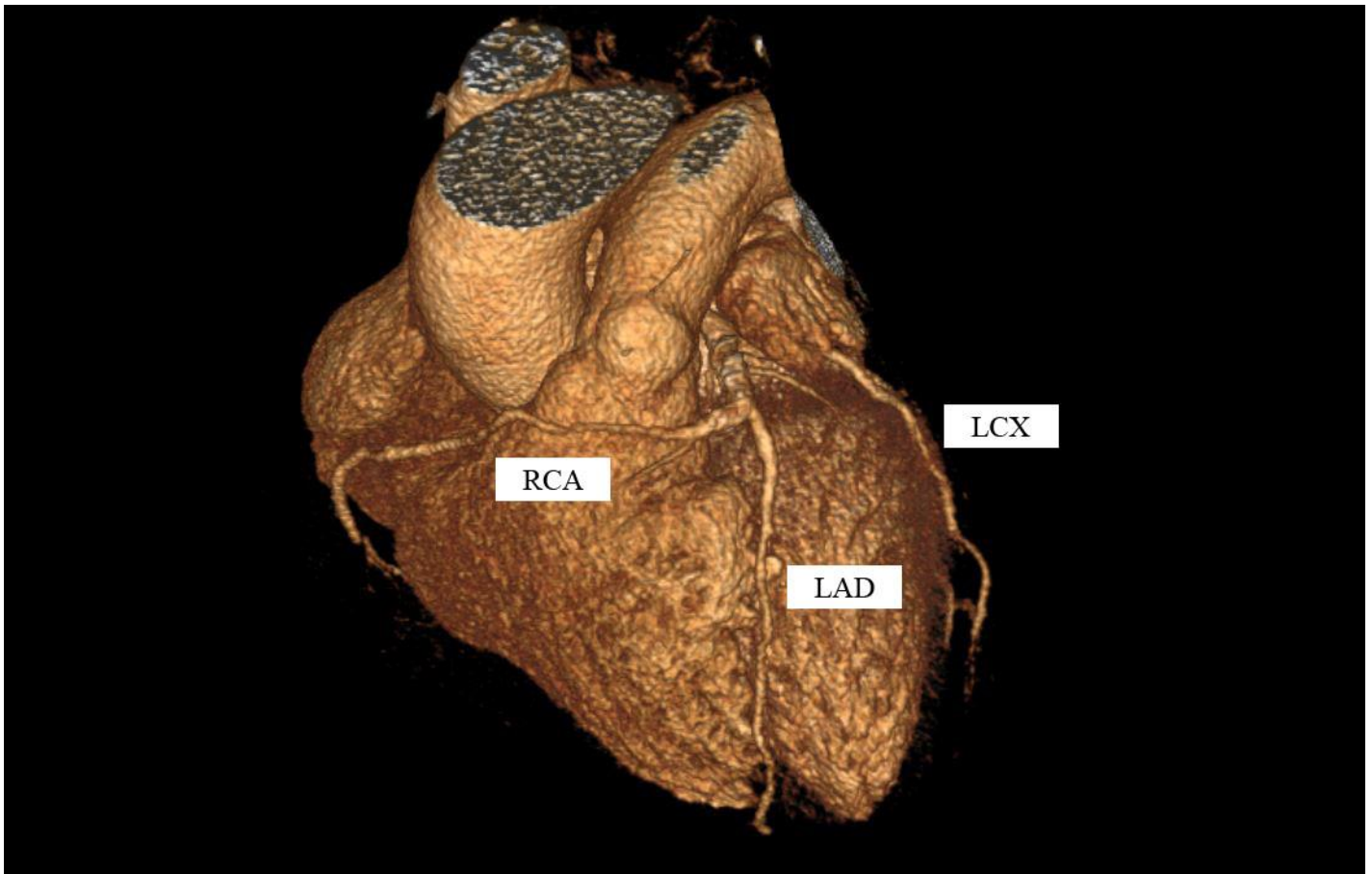
Figure 2: 3D reconstruction of CTA coronary shows anomalous RCA, which originates from the mid-portion of LAD and courses anterior to the pulmonary trunk into the right atrioventricular groove.

Penumbra

62
68
72

RED™

REPERFUSION CATHETERS

REDglide™ Technology

Designed to enhance delivery in tortuosity

62
.062" ID
1.93mm (0.76") OD
138cm Length

68
.068" ID
2.13mm (0.84") OD
132cm Length

72
.072" ID
2.16mm (0.85") OD
132cm Length